Extended data for

Observation of unconventional van der Waals multiferroics near room temperature

Yangliu Wu[1], Haipeng Lu[1], Xiaocang Han[2], Chendi Yang[3], Nanshu Liu[5], Xiaoxu Zhao[2], Liang Qiao[4], Wei Ji[5], Renchao Che[3], Longjiang Deng[1]* and Bo Peng[1]*

[1]National Engineering Research Center of Electromagnetic Radiation Control Materials, School of Electronic Science and Engineering, University of Electronic Science and Technology of China, Chengdu 611731, China

[2]School of Materials Science and Engineering, Peking University, Beijing 100871, China

[3]Laboratory of Advanced Materials, Department of Materials Science, Collaborative Innovation Center of Chemistry for Energy Materials(*iChEM*), Fudan University, Shanghai 200433, China

[4]School of Physics, University of Electronic Science and Technology of China, Chengdu 611731, China

[5]Beijing Key Laboratory of Optoelectronic Functional Materials & Micro-Nano Devices, Department of Physics, Renmin University of China, Beijing 100872, China

The PDF file includes:

Supplementary Text

(Extended Data Fig. 1 to 20)

References (49-50)

Supplementary Text

Part A: KAI model and Merz's law

The switching dynamics of ferroelectric materials is typically described by Kolmogorov-Avrami-Ishibashi (KAI) model. The normalized change in electric polarization can be expressed by the compressed exponential function[46]

$$\Delta P(t) / 2P_r = 1 - \exp\left[-(\frac{t}{\tau})^n \right]$$

$$-\ln(1 - \Delta P(t) / 2P_r) = (\frac{t}{\tau})^n \quad (1)$$

where τ is a characteristic switching time. In the conventional KAI model, the index n depends on the dimensionality of the domains; the value is 2 for 2D thin films and 3 for 3D single crystals. The switching time follows the empirical Merz law

$$\tau = \tau_f \exp\left(\frac{E_{a,t}(T)}{E} \right)$$

$$\ln(\tau) = E_{a,t}(T) \cdot \frac{1}{E} + \ln(\tau_f) \quad (2)$$

where τ_f is the switching time of domain-wall under an infinite field, E is the applied electric field and $E_{a,t}$ is the temperature-dependent activation field.

The $\Delta P(t)$, P_r and corresponding time t extract from frequency (f) dependence of P-E loops at different electric fields and temperatures. The $-\ln(1-\Delta P(t)/2P_r)$ as a function of corresponding time ($t = 1/4f$) at various electric fields and temperatures are presented in Extended Data Fig. 16. The solid lines are fits to the compressed exponential function of Eq. (1). An excellent agreement is observed. The Avrami index n and the switching time τ are obtained from the fitting parameters. The extracted values of the $\ln(\tau)$ as a function of the reciprocal of electric field at various temperatures are presented in Fig. 2i. The solid lines are fits to the empirical Merz's law as given by Eq. (2). The Avrami index n as a function of electric field at temperatures between 230 and 295 K is shown in Extended Data Fig. 16e. The Avrami index monotonically increases from 1 to 1.7 with both increasing electric field and increasing temperature, which indicates that the ferroelectric domains in the trilayer NiI_2 exhibit one-dimensional growth at low electric fields and tend to two-dimensional growth at high electric fields. Alternatively, domain nucleation and growth evolve to be isotropic with increasing temperature. This behavior is similar to the previous report on three-dimensional ferroelectricity[49], showing that the Avrami index n increases from ~1 to 3 with increasing electric field and temperature.

Part B: Magnetic control ferroelectric switching ranging from 10 to 295 K

In our experiment, the magnetic control of ferroelectric switching was measured at a fixed low electric field of 0.74 MV/cm. It is shown that the $-\ln(1-\Delta P(t)/2P_r)$ as a function of time is linear, as presented in Fig. 4d and Extended Data Fig. 20. These results are characterized by an Avrami index of 1, which indicate that the ferroelectric polarization domains grow in a 1D fashion. In the range of 10 K to 295 K, the magnetic field exhibits a deceleration effect on the ferroelectric switching, which is consistent with the observed red-shift of resonance peaks in Fig. 4c and Extended Data Fig. 19.

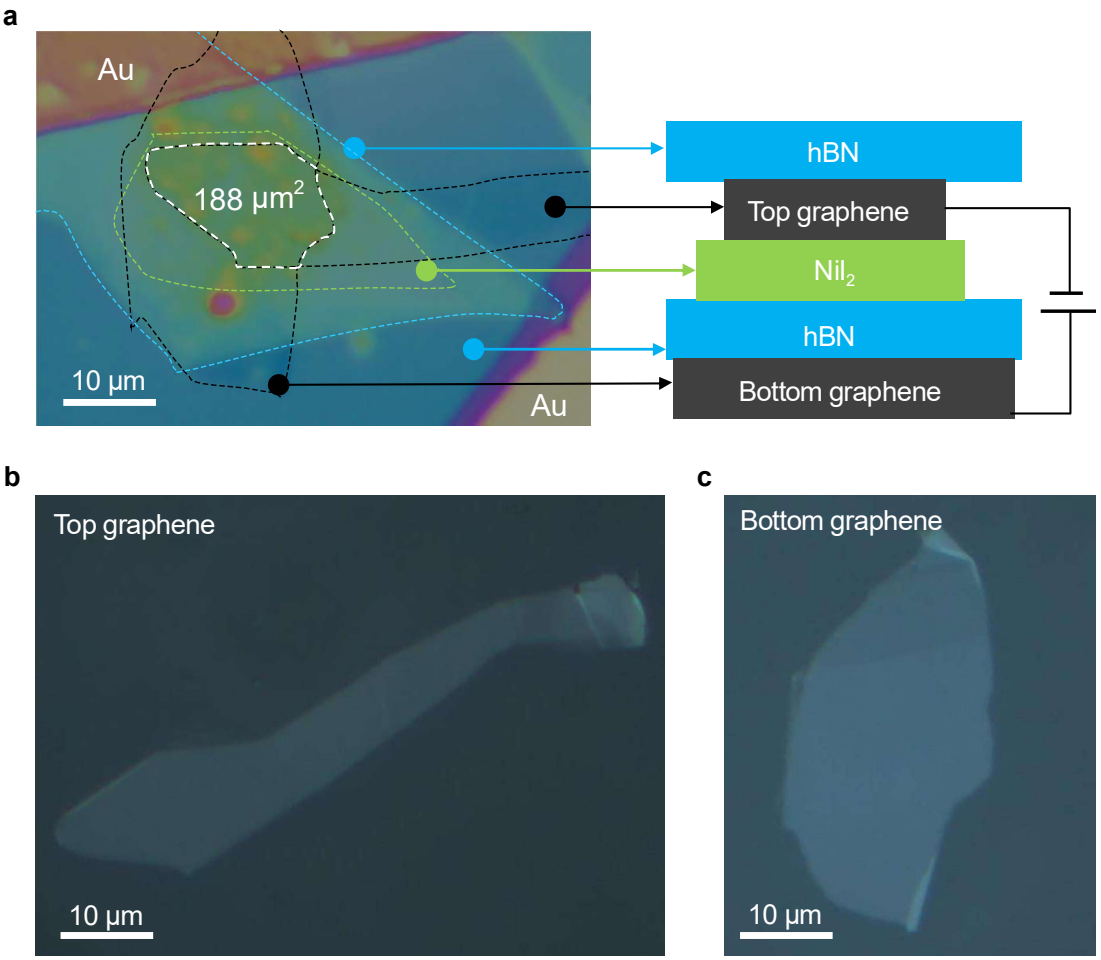

Extended Data Fig. 1 | Trilayer NiI_2 device. a, Optical micrograph (left) and schematic side view (right) of a trilayer NiI_2 sample on hBN substrate and covered by graphene and another hBN on the top. The white dashed line indicates the area of trilayer NiI_2 between two graphene electrodes, which were contacted with Au electrodes through a PDMS dry transfer method and further directly connected with ferroelectric tester (Precision Premier II: Hysteresis measurement) and voltage source meter. **b, c,** The optical micrograph of top and bottom graphene as electrodes. The area of NiI_2 sandwiched by top and bottom graphene electrodes is estimated to be ~188 μm^2 by grid segmentation method.

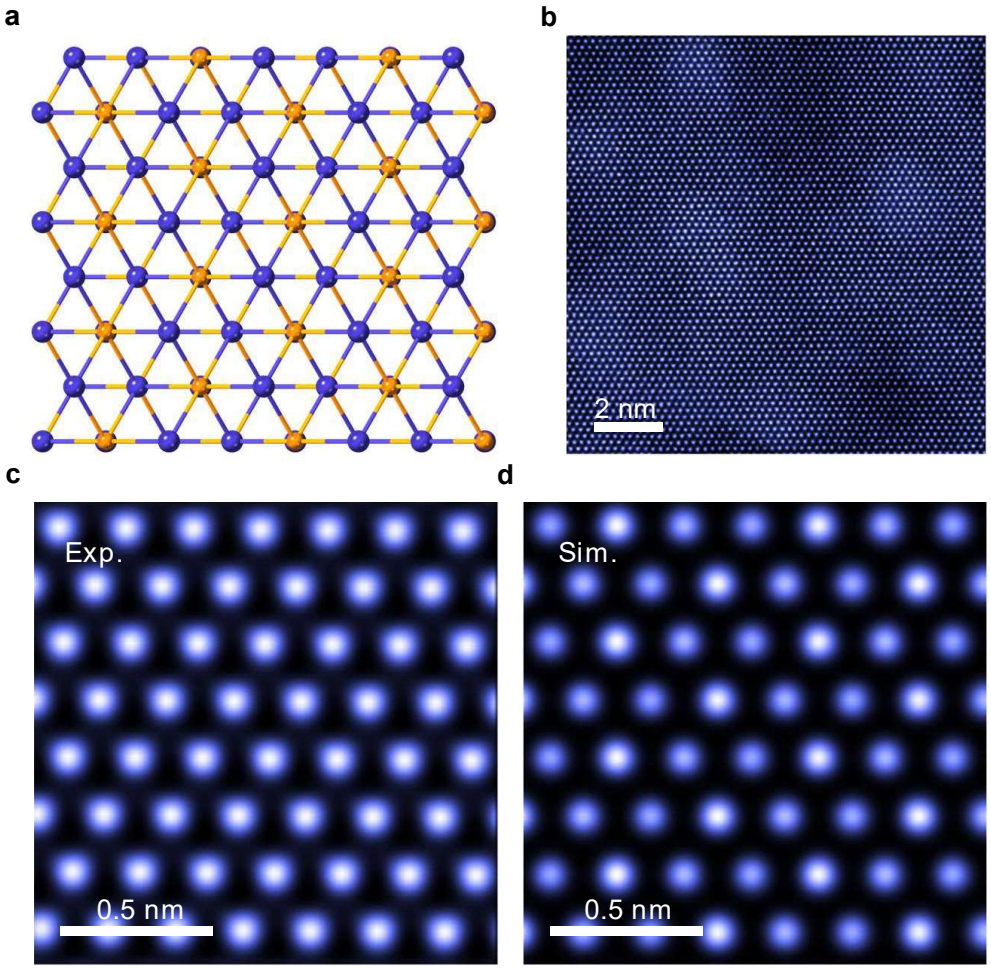

Extended Data Fig. 2 | Atomic structures of few-layer NiI_2. a, The atomic models of layered NiI_2 viewed along the c axis. Blue and orange spheres represent iodine ions and nickel ions, respectively. **b-d,** The atomic-resolution ADF-STEM images of few-layer NiI_2 and corresponding simulated images.

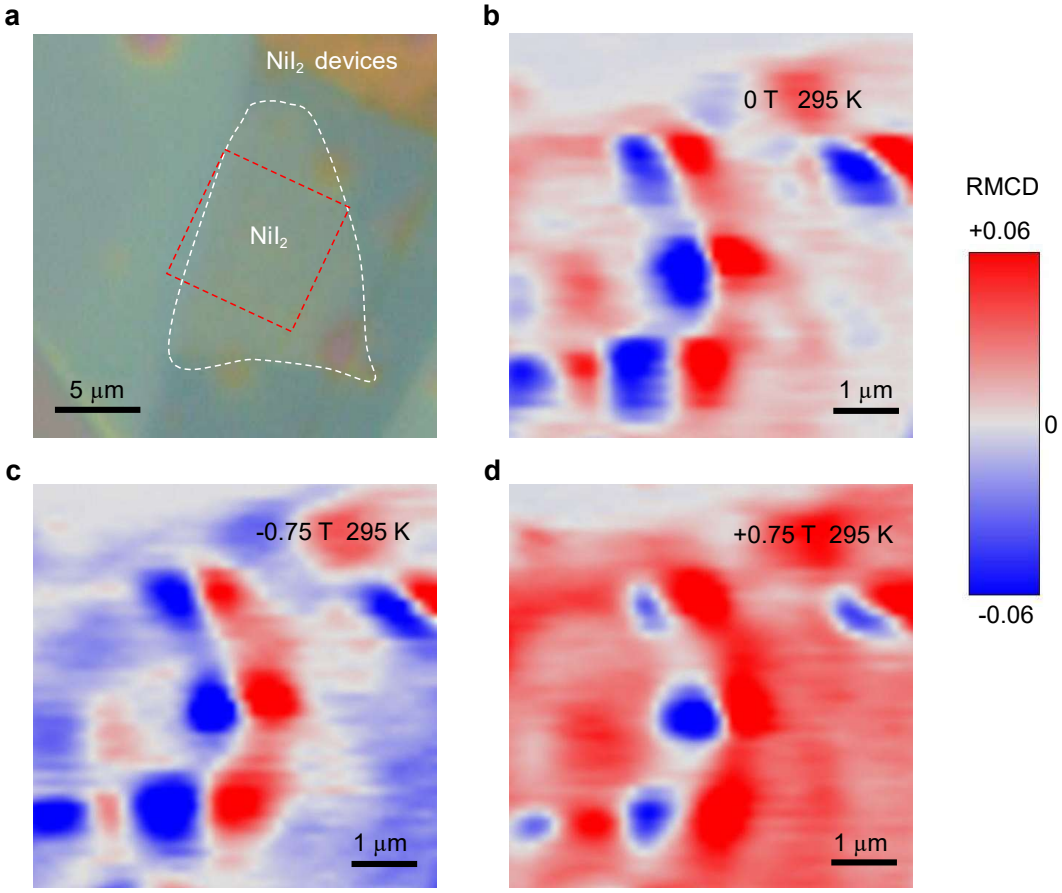

Extended Data Fig. 3 | Magnetic texture in few-layer NiI_2 encapsulated by hBN at 295 K. **a,** Optical micrograph of another few-layer NiI_2 put on hBN substrate and further covered by another hBN on the top. The white and red dashed-line box represents the profile of the NiI_2 flake and the area of RMCD maps. **b-d,** Polar RMCD maps at 295 K, taken at selected out-of-plane magnetic field.

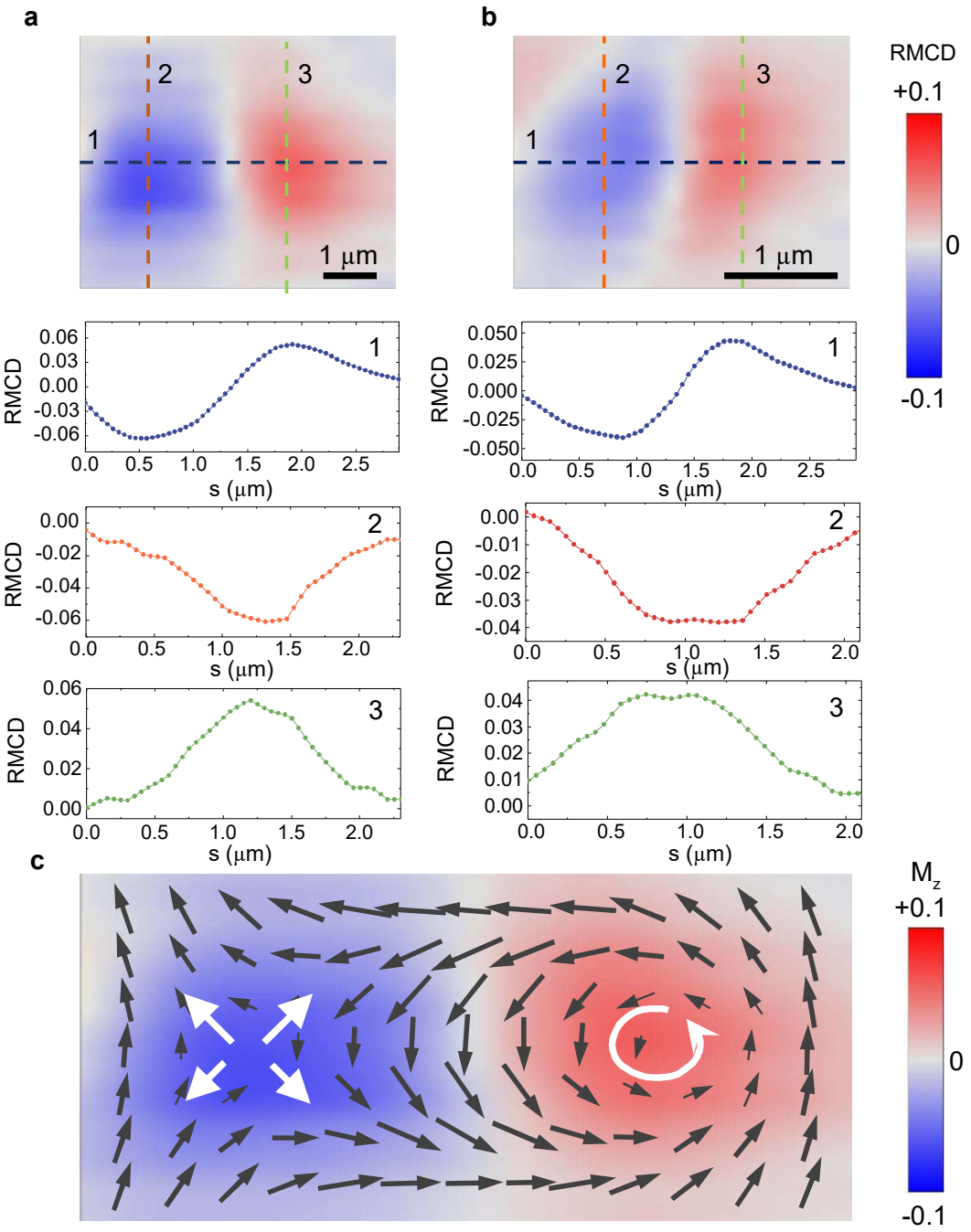

Extended Data Fig. 4 | Magnetic structure of domains in trilayer NiI_2 at 295 K and 0 T. a-b, The local RMCD images (top panel) along with the line sections of RMCD signals (bottom panel) indicate that isolated bimerons-like domains in trilayer NiI_2 at 295 K and zero magnetic field. **c,** Schematic of the spin textures of bimerons-like domains and corresponding zoom-in RMCD images.

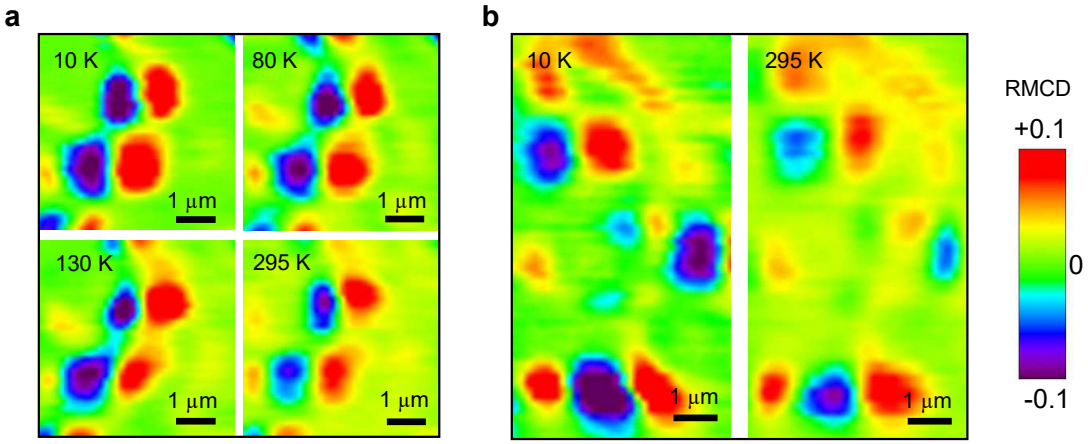

Extended Data Fig. 5 | The temperature-dependent RMCD maps of trilayer and another few-layer NiI_2 at 0 T. To see more details, the polar RMCD maps are presented in multiple colors. The RMCD maps of the few-layer (**a**) and trilayer samples (**b**) clearly shows that the bimerons-like domains shrink with increasing temperature.

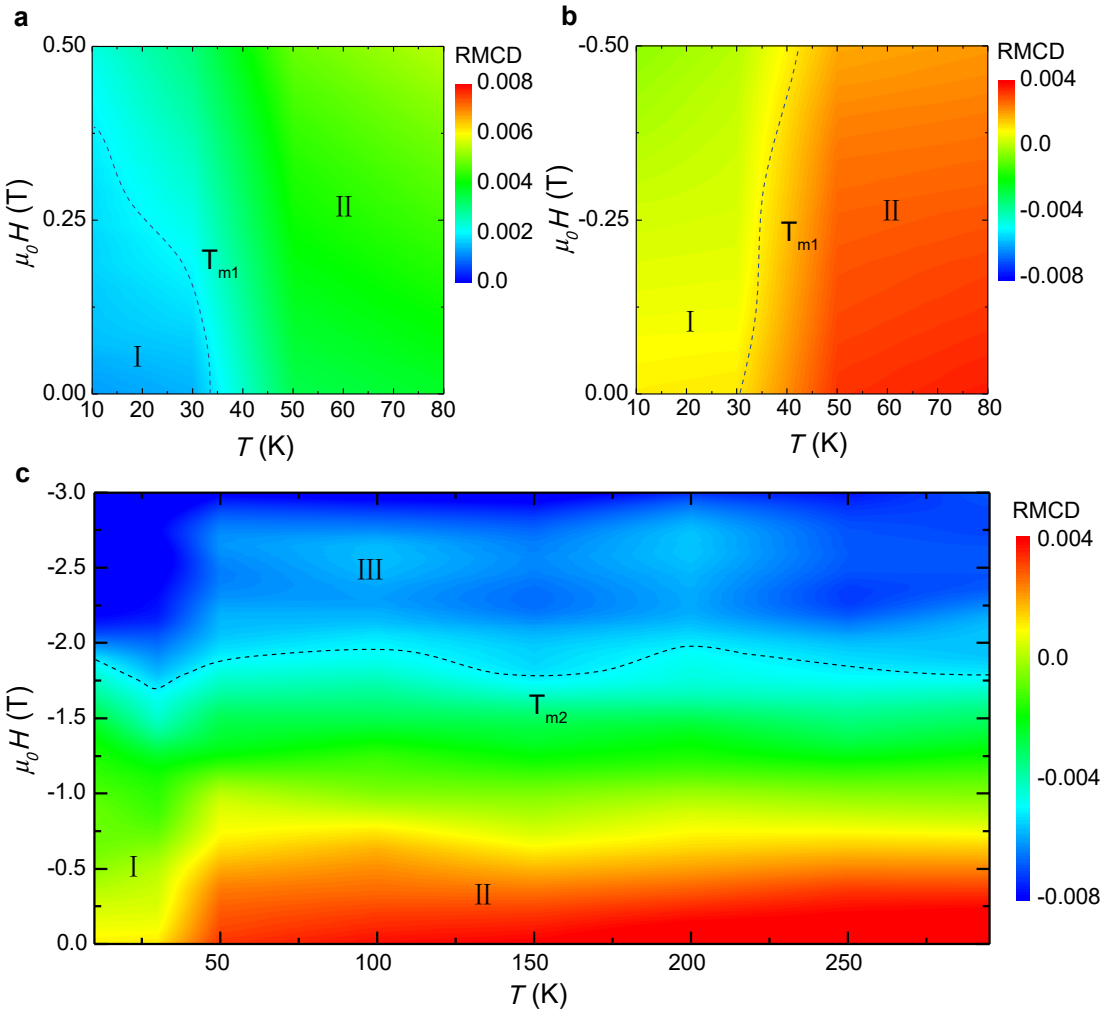

Extended Data Fig. 6 | The magnetic phase diagram of trilayer NiI_2. a-c, The RMCD intensity as a function of magnetic field and temperature. The magnetic transition temperature T_{m1} and T_{m2} marked by the dashed line, and the antiferromagnetic order appears below the T_{m1} line. The dashed lines are guidelines for the eyes.

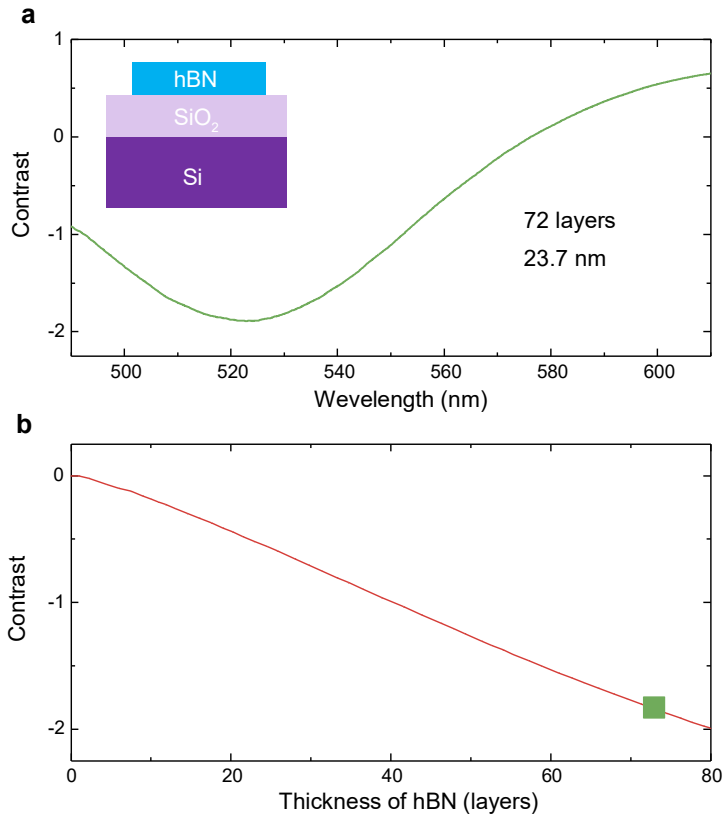

Extended Data Fig. 7 | Thickness of hBN in device. a, The optical contrast of bottom hBN on SiO_2/Si substrate as a function of the wavelength of light, which was applied to guarantee non-contact between bottom graphene electrode and trilayer NiI_2 for the ferroelectric measurements. **b,** The optical contrast at 516 nm varies linearly with the thickness of the hBN nanoflake between 1 and 80 layers[50]. The optical contrast at 516 nm indicates that the bottom hBN is approximately 72 layers, as shown in the light green square.

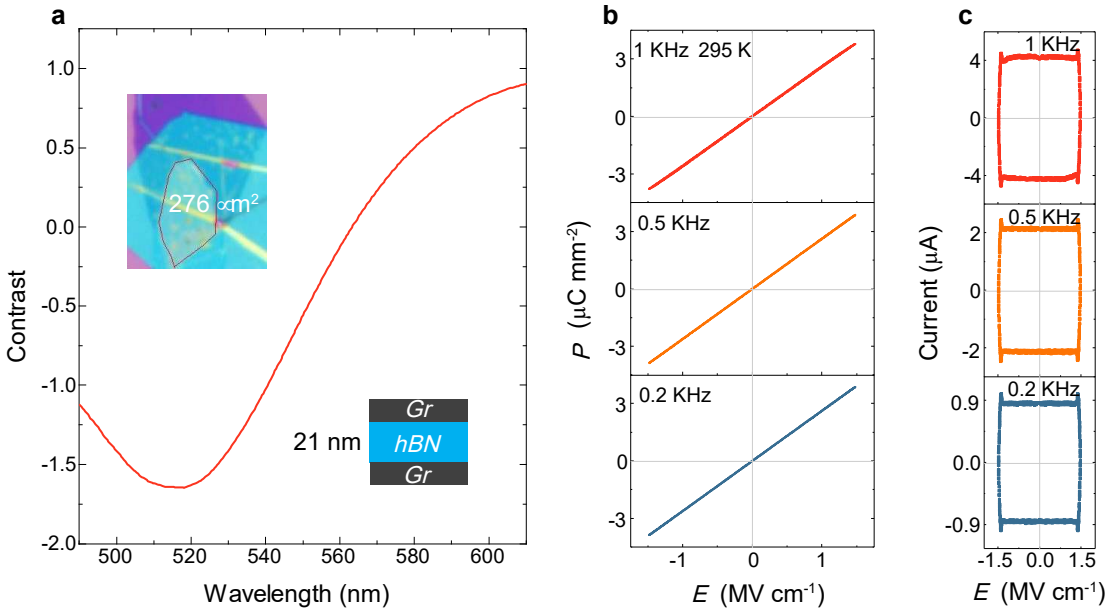

Extended Data Fig. 8 | Background signals from hBN flake. a, The optical contrast of a pristine hBN flake composing a graphene/hBN/graphene device to check the electric properties of pristine hBN as control experiments. The selected pristine hBN flake is around 21 nm thickness, close to that in trilayer NiI_2 device. The insets show the optical microscopy image and device schematic. **b-c,** The Raw *P*-*E* and *I*-*E* loops of pristine hBN devices at various frequency at 295 K. The pristine hBN shows a linear behavior with electric field, suggesting pristine hBN is an excellent insulator without ferroelectric polarization.

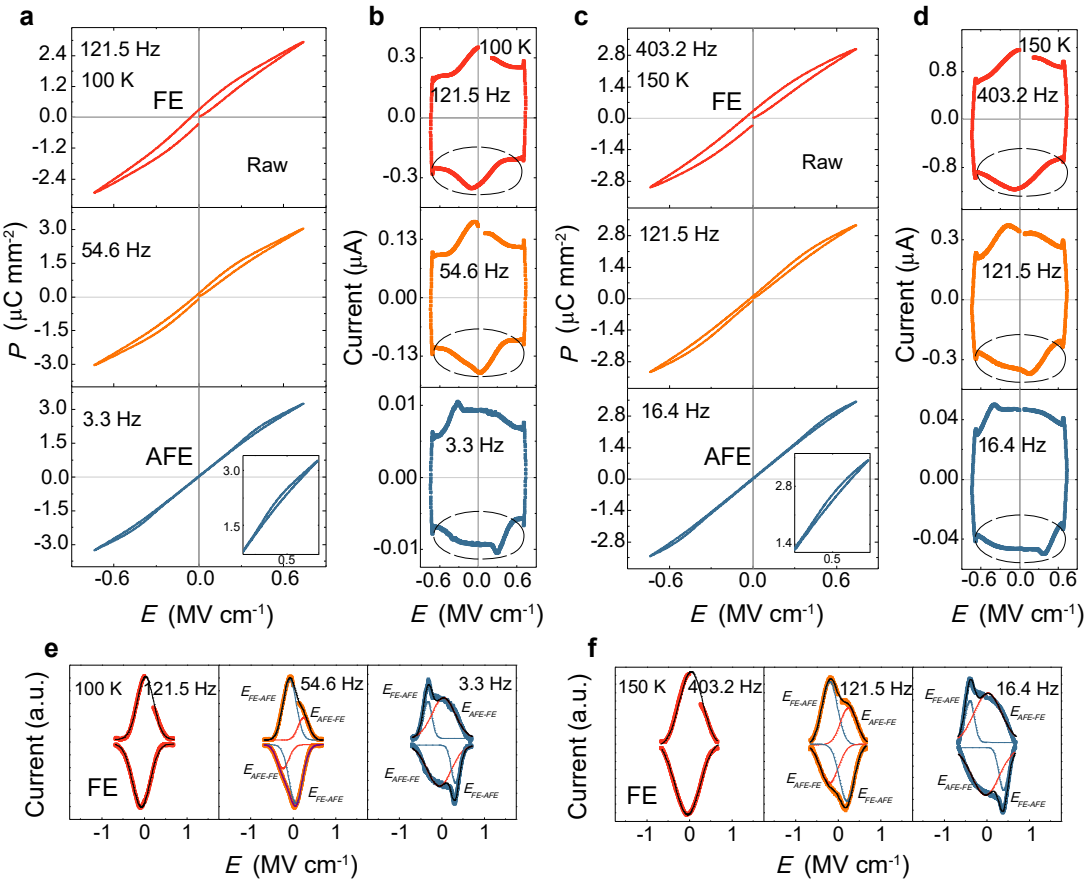

Extended Data Fig. 9 | Coexistence of FE and AFE orders in trilayer NiI_2. Raw *P-E* and *I-E* loops as a function of the frequency of applied electric field at various temperatures (Device 1): **a, b,** 100 K, **c, d,** 150 K. The insets in (**a**) and (**c**) show the enlarged *P-E* loops. **e, f,** Corresponding *I-E* curves of (**b, d**) after subtracting the current background, fitted by Gaussian function. As decreasing frequency, a single-hysteresis loop of FE features along with a pair of opposite switching current peaks, evolves to a characteristic slim double-hysteresis loop of AFE polarization, typically with two pairs of switching current peaks and decreasing P_r. This suggests that an evolution from FE to AFE takes place.

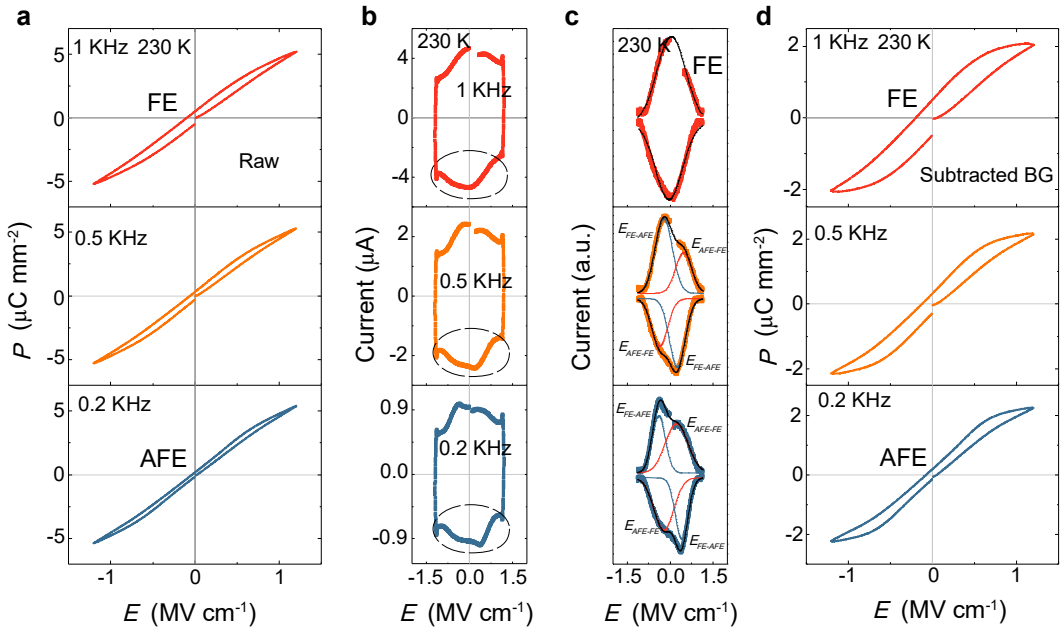

Extended Data Fig. 10 | Ferroelectric polarization at 230 K. a, b, Raw *P-E* and *I-E* loops at various frequencies and 230 K (Device 1). **c, d,** Corresponding *I-E* and *P-E* curves after subtracted the background (BG). The features of FE polarizations are observed (**a**), particularly, the *P-E* loops subtracted BG show more vivid ferroelectric hysteresis behaviors (**d**). The *I-E* loops show an evolution from one pair of switching current peaks to two pairs (**b, c**), which indicates an evolution from FE to AFE. The two pairs of current peaks originate from FE-AFE and AFE-FE switching (**c**), fitted by Gaussian function.

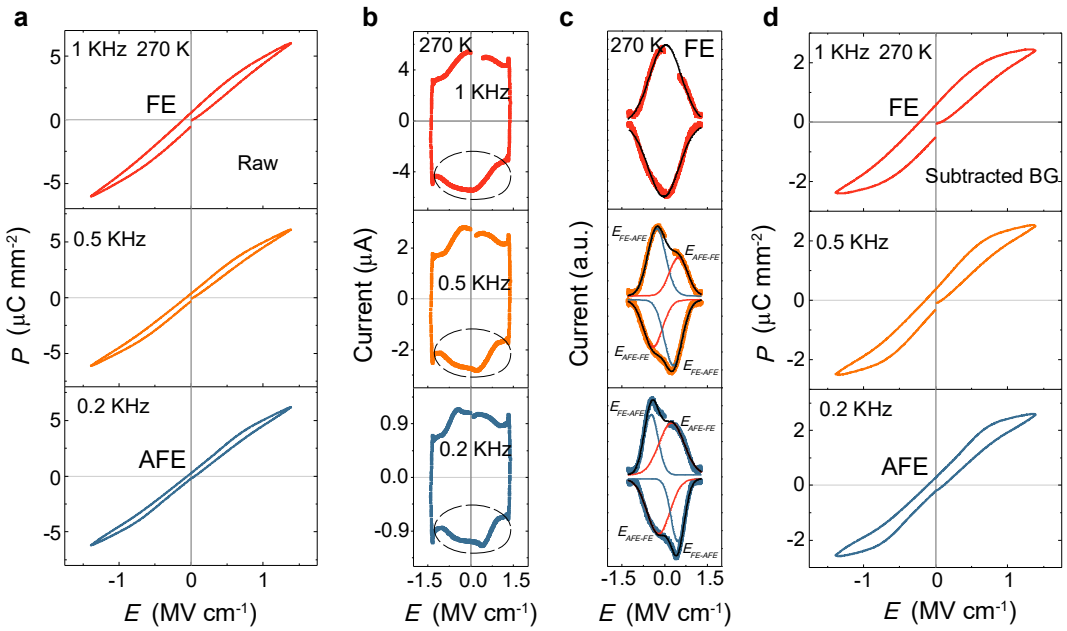

Extended Data Fig. 11 | Ferroelectric polarization at 270 K. a, b, Raw *P-E* and *I-E* loops at various frequencies and 270 K (Device 1). **c, d,** Corresponding *I-E* and *P-E* curves after subtracted the background (BG). The features of FE polarizations are observed, particularly, the *P-E* loops subtracted BG show more vivid ferroelectric behaviors (**d**). The *I-E* loops show an evolution from one pair of switching current peaks to two pairs (**b, c**), which indicates an evolution from FE to AFE. The two pairs of current peaks originate from FE-AFE and AFE-FE switching (**c**), fitted by Gaussian function.

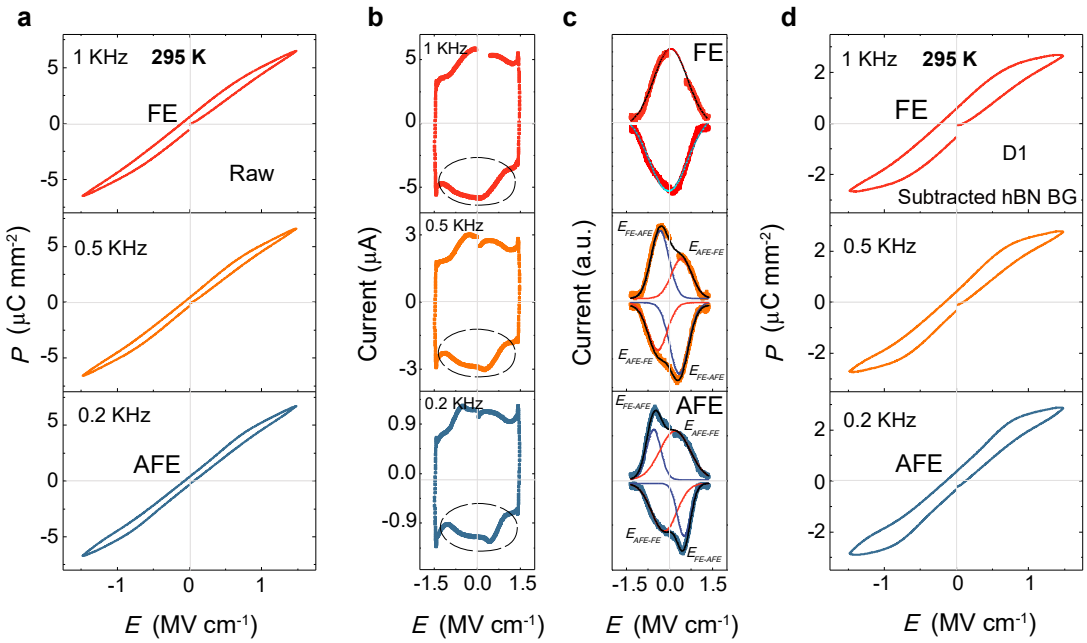

Extended Data Fig. 12 | Ferroelectric of Device 1 at 295 K. a, b, Raw *P-E* and *I-E* loops at various frequencies and 295 K (Device 1). **c, d** Corresponding *I-E* and *P-E* curves after subtracted the hBN background (Extended Data Fig. 8). The features of ferroelectric polarizations are observed, particularly, the treated *P-E* loops show more vivid ferroelectric hysteresis behaviors (**d**). The *I-E* loops show an evolution from one pair of switching current peaks to two pairs (**b, c**), which indicates an evolution from ferroelectric to anti-ferroelectric. The two pairs of current peaks originate from FE-AFE and AFE-FE switching (**c**), fitted by Gaussian function. This result confirms that the ferroelectric polarization is persisted to near room temperature.

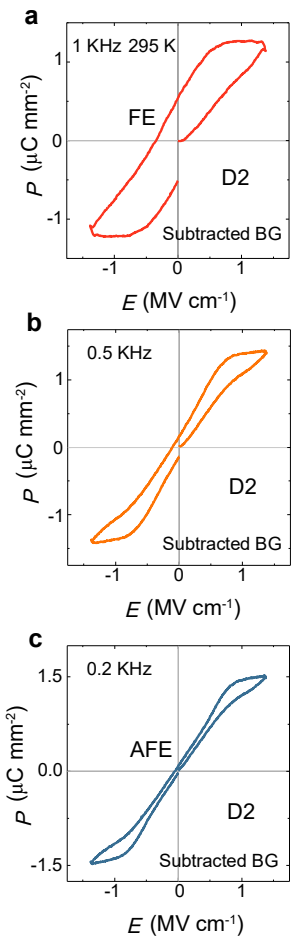

Extended Data Fig. 13 | Ferroelectric at 295 K in Device 2. Corresponding *P*-*E* curves after subtracting the current background at various frequencies: (**a**) 1 KHz, (**b**) 0.5 KHz, (**c**) 0.2 KHz, which showing more vivid ferroelectric hysteresis behaviors and endorse the finding of the near-room-temperature ferroelectric.

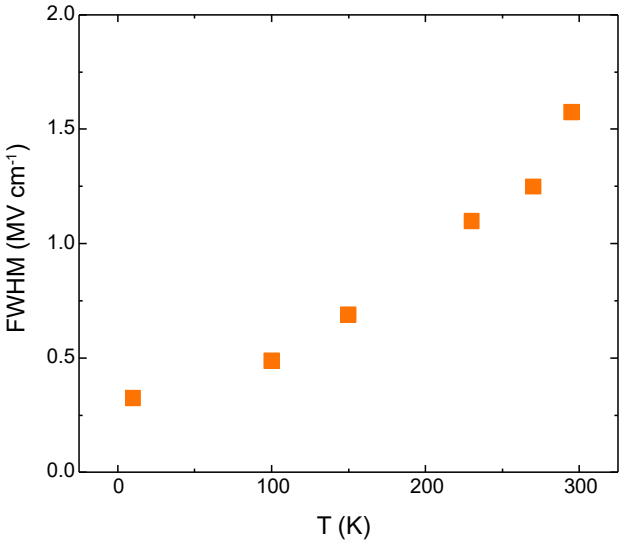

Extended Data Fig. 14 | Broadening switching current peak as a function of temperature. The FWHM (full width at half maximum) of switching current single peak of FE polarization (Device 1), obtained from Fig. 3e, Extended Data Fig. 9e-f, Extended Data Fig. 10-12c. As the temperature increase to 295 K, the switching current peaks are broadened by around 5 times compared with that at 10 K.

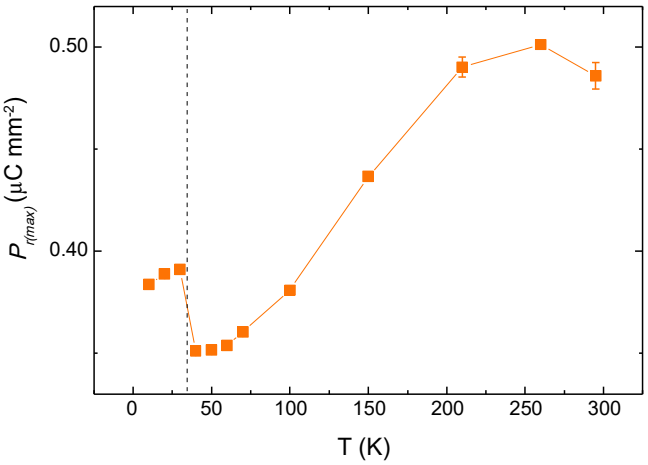

Extended Data Fig. 15 | Phase transition of ferroelectric linked with magnetic orders. P_r^+ at resonance frequency ($P_{r(max)}$) as a function of temperature, extracted from Fig. 3g. A FE phase transition takes place at around 35 K, consistent with the magnetic phase transition. The error bars are standard deviations of $P_{r(max)}$.

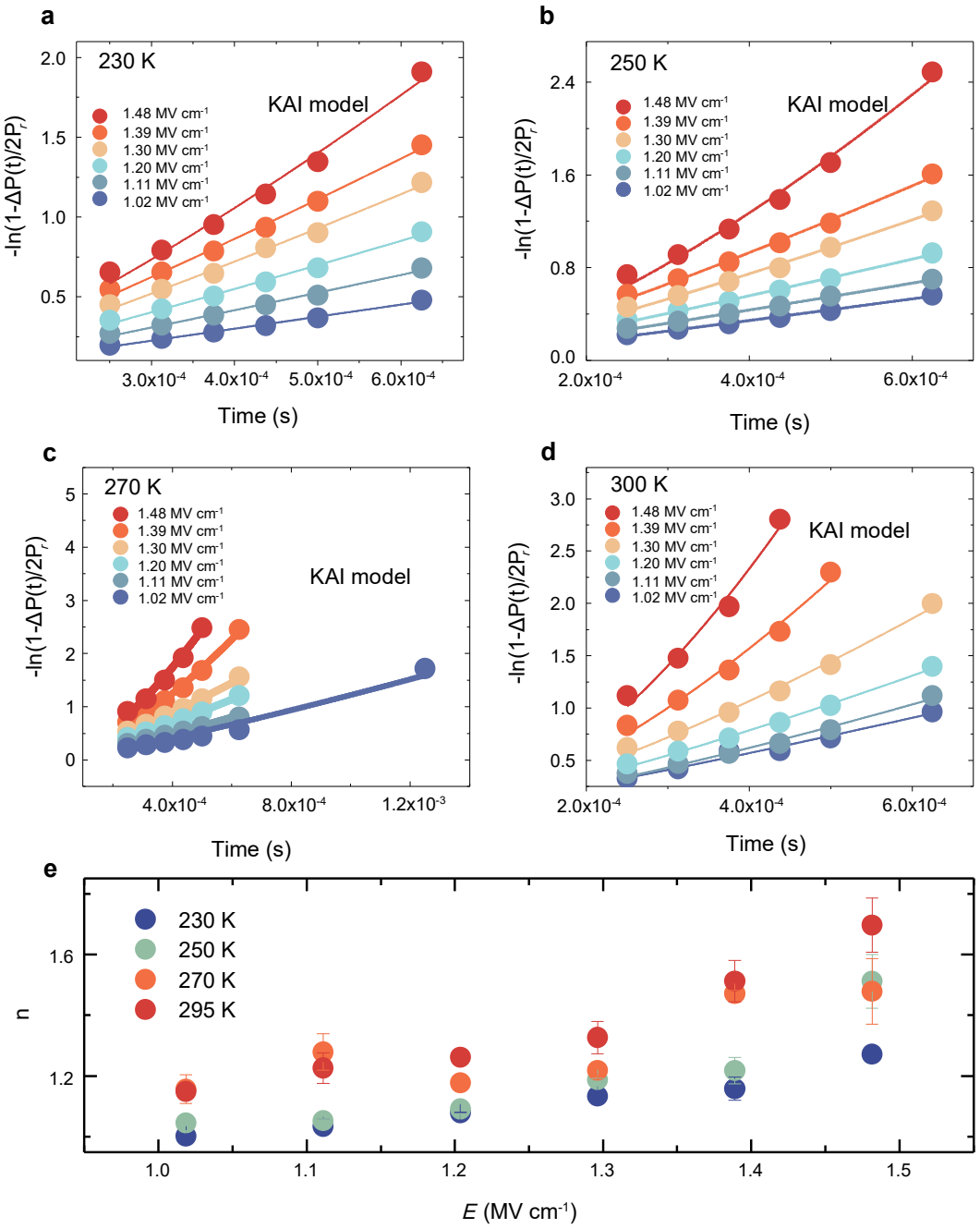

Extended Data Fig. 16 | KAI model. a-d, Experimental results (solid circle) fitted by KAI model (solid line) at different temperatures and electric field (Part A). **e,** Calculated Avrami index *n* through KAI model as a function of electric field at different temperatures.

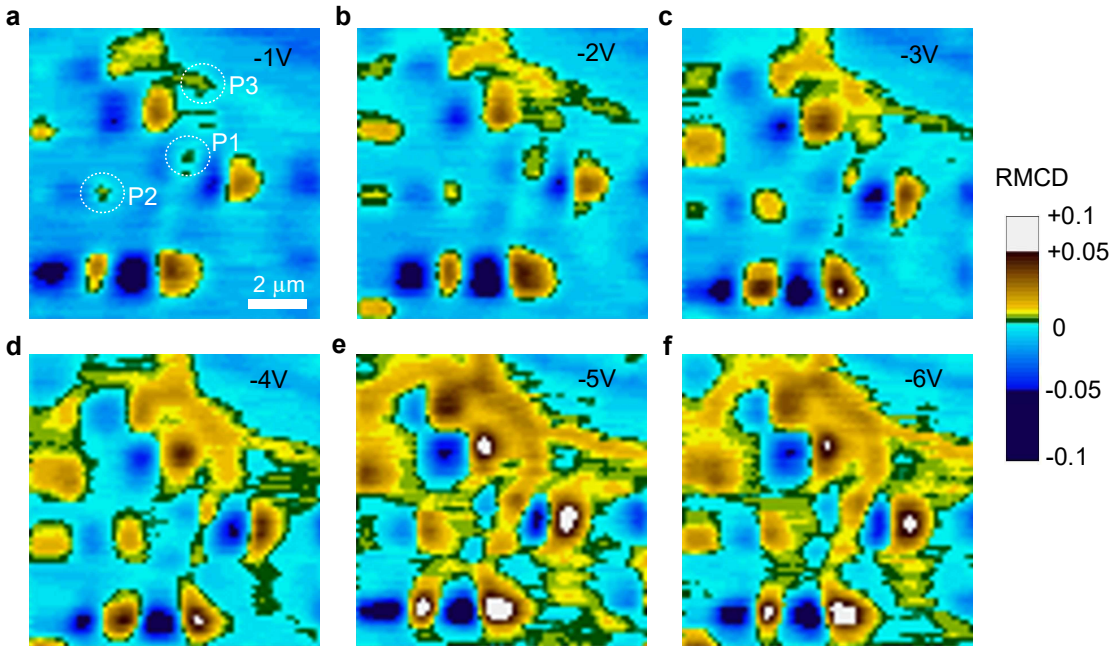

Extended Data Fig. 17 | Electrical control of magnetic domains in trilayer NiI_2 at 295 K. Polar RMCD maps as a function of applied voltage ranging from -1 V (-0.37 MV/cm) to -6 V (-2.22 MV/cm), taken at 0 T and 295 K. The white dashed circles highlight the typical three individual magnetic domains.

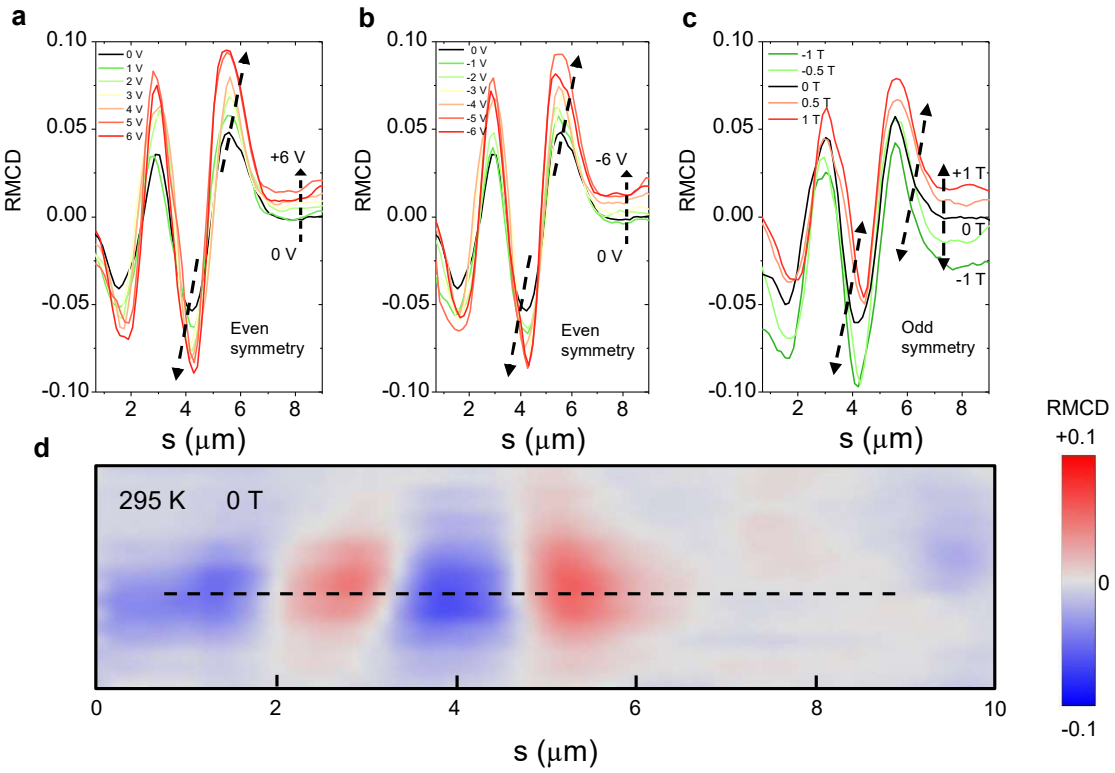

Extended Data Fig. 18 | Electrical control of bimeron-like domains at 0 T and 295 K. a, b, The polar RMCD signals along with the line sections of RMCD map (**d**) as a function of electric field. The RMCD intensities increase as both positive and negative electric field increase. **c,** The RMCD signals along with the line sections of RMCD map (**d**) as a function of magnetic field. The black dashed arrow indicates the opposite changing trend of the magnetization component of "core-down antivortex" and "core-up vortex" as a function of the magnetic field. **d,** The polar RMCD map for two pair of bimeron-like domains.

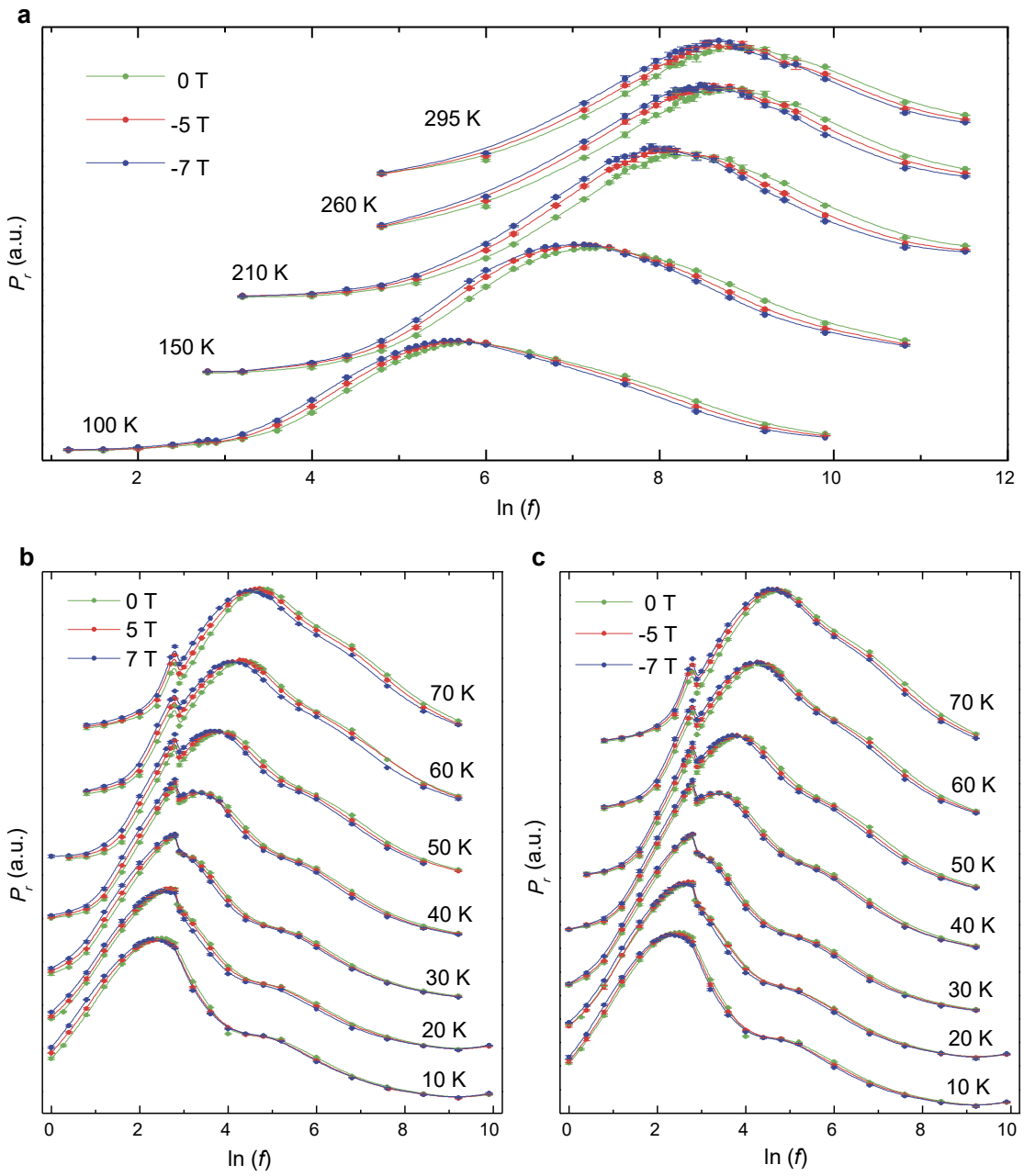

Extended Data Fig. 19 | Magnetic control of ferroelectric switching. a-c, P_r as a function of the natural logarithm of frequency (f) at different temperature and magnetic field. The error bars are standard deviations of P_r. The magnetic field induces a redshift of resonance frequency peaks and a decrease of ferroelectric switching frequency.

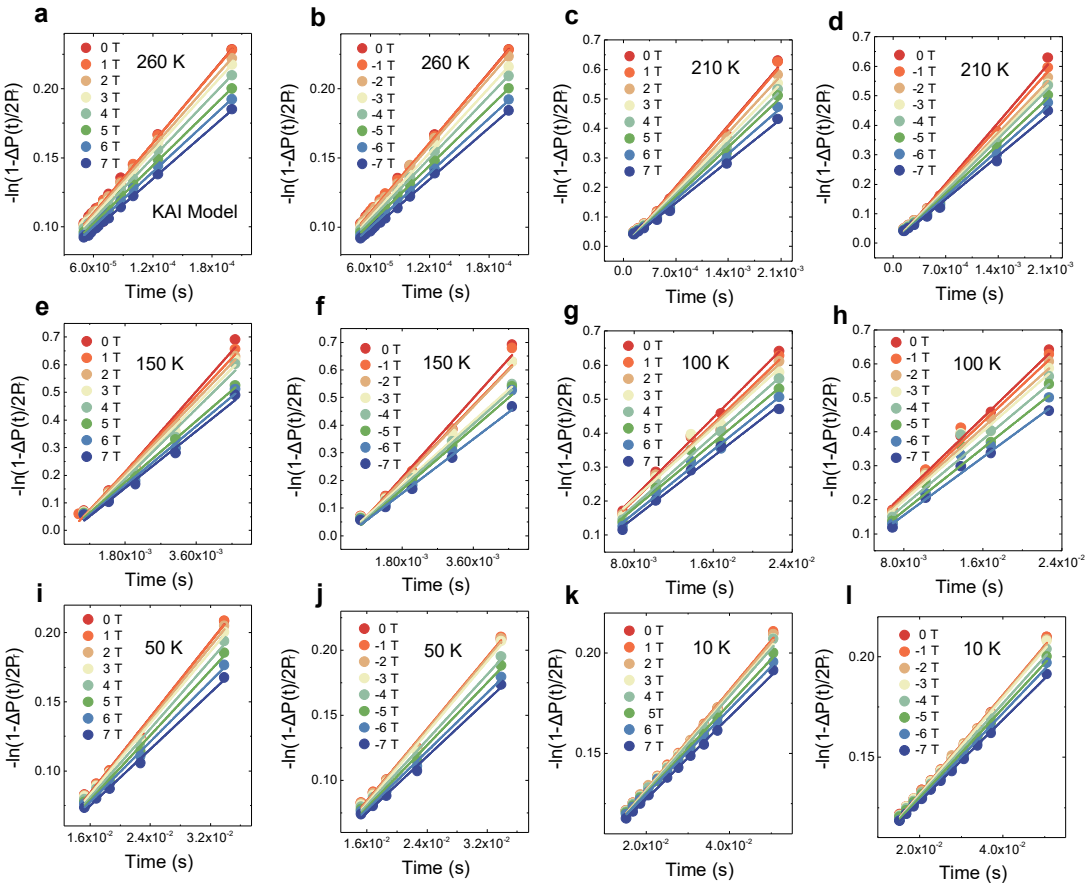

Extended Data Fig. 20 | Characteristic switching time at various temperatures and magnetic fields. a-l, Experimental results (solid circle) fitted by KAI model (solid line) at different magnetic fields and temperature (Part A and B), while electric field is fixed at 0.74 MV/cm. The characteristic switching time increase with increasing magnetic field.

Reference:

49. Hu, W. J. et al. Universal ferroelectric switching dynamics of vinylidene fluoride-trifluoroethylene copolymer films. Sci. *Rep.* **4**, 4772 (2014).

50. Golla, D. et al. Optical thickness determination of hexagonal boron nitride flakes. *Appl. Phys. Lett.* **102**, 161906 (2013).